CFD modeling and performance evaluation of multipass solar air heaters

Al-Damook, M., Obaid, Z. H., Al Qubeissi, M., Dixon-Hardy, D., Cottom, J. & Heggs, P. J.

CFD modelling and performance evaluation of multi-pass solar air heaters

Abstract – This paper investigates the impacts of flow configurations on the thermal performance of a solar heater system. Recycled aluminium cans (RAC) have been utilised as turbulators with a double pass single duct solar air collector. CFD software of COMSOL Multiphysics V5.3a is used to model three designs: co-current (model A), counter-current (model B), and U-shape (model C). The numerical results show that the U-shape design offers 5.4% and 6.5%, respectively, greater thermal performance compared with the co-current and counter-current flow models. An outdoor experiment is performed based on the numerical modelling of flow configurations. The experimental setup is examined for three configurations of model C, namely, solar air heater (SAH) without RAC model C-I (plain model), SAH with in-line RAC layout (model C-II), and SAH with staggered RAC layout (model C-III). Furthermore, the double pass single duct solar air collector (model C) design is in a good agreement with the experimental data. The experimental study reveals that model C-III has a better thermal efficiency of 60.2%, compared to those of model C-II, 53.1%, and model C-I, 49.4%.

Keywords: Recycled cans; CFD; Absorber plate; Duct flow; Power fan; Solar collector.

Nomenclature

Symbol	Quantity	SI Unit
A	Area	m²
c_p	specific heat capacity	J kg^{-1} k^{-1}
D	diameter	M
E	percentage error	
G	global solar radiation	W m^{-2}
H	heat transfer coefficient	W m^{-2} K^{-1}
k	thermal conductivity	W m^{-1} K^{-1}
l	turbulence length scale	M
$\mathcal{L}$	airflow path length from inlet to outlet	M

$\dot{m}$	mass flowrate	kg s^{-1}
P	power	W
Pe	perimeter (wetted perimeter)	M
Q_{vd}	viscous dissipation	W
$\dot{Q}$	heat rate	W
T	Temperature	K
U	overall heat transfer coefficient	W m^{-2} K^{-1}
$\bar{V}$	mean (uniform) velocity	m s^{-1}
u	velocity component in x-direction	m s^{-1}
v	velocity component in y-direction	m s^{-1}
V	total velocity vector	m s^{-1}
$\dot{V}$	flow rate	m^3 s^{-1}
w	velocity component in z-direction	m s^{-1}

Greek symbols

σ	Stefan-Boltzmann constant (5.67 × 10 $^{-8}$)	W m^{-2} K^{-4}
β	tilt angle	Rad
μ	dynamic viscosity	kg m^{-1} s^{-1}
δ	depth of flow	M
ϕ	independent fluid property	
ρ	Density	kg m^{-3}
υ	kinematic viscosity	m^2 s^{-1}

Non-dimensional Numbers

f	Fanning friction factor
gf	geometry factor
Pr	Prandtl number, $c_p \mu / k$
Re	Reynolds number, $4\dot{m}/\mu\, p$
F	friction factor
E	Emissivity
η	Efficiency
τ	solar transmissivity

Subscripts and superscripts

Amb	ambient
B	bottom
Bs	back surface of solar collector
C	cross-sectional, or characteristic value
D	depth
F	fluid domain or fan
Fm	mean fluid
G	Glass
H	Hydraulic
i	Inlet

Ins	insulation
o	Outlet
P	Plate
R	Radiation
S	solar or surface
Th	thermal
U	useful heat gain
w	Wind

Abbreviations

AEQ	average element quality
Al	Aluminium
CFD	computational fluid dynamics
Cu	Copper
RMSE	root-mean-square error
PPMCC	Pearson correlation coefficient
RAC	recycled aluminium can(s)
SAH	solar air heater(s)
RT	Relative tolerance

1. Introduction

Solar air heaters (SAH) have been utilized in many industrial and domestic applications; for example, space heating and in drying processes for agricultural products, herbal medicines, and clothing [1, 2]. The performance of SAH is influenced by the collector geometry (depth flow and length of collector), type of absorber surface (colour, roughness and material), glass cover plate [3] (thickness, material and transparency), and type of flow regime (turbulent or laminar) [4-8]. Increasing the heat transfer rate of the SAH can be achieved by either increasing the absorber surface area or increasing the airflow [9]. While the latter will increase the heat transfer losses to the surroundings [10], they will also increase the pressure drop across the collector. A compromise approach is to use heat transfer augmentation techniques to the flat plate solar air collector, such as introducing turbulators into the air channel duct [11].

Many attempts were made to improve the performance of a double pass solar air heater by integration with extended surfaces (obstacles, fins, or turbulators) [12-16]. For

example, some attempts were made to cause air turbulence in the channels using baffles or ribs [17, 18]. In [19], the presence of obstacles in the air channels had significant impact for improving the SAH thermal efficiency. This was attributed to the increase of heat transfer surface area along airflow around the fin absorbing plates. Prabha and Sharma [20] showed substantial improvement in the thermal efficiency from 43% to 61% at a mass flowrate of $0.011 \, \mathrm{kg. \, s^{-1}}$ with the fin spacing decreased from 4 cm to 1 cm. In [21], a double pass SAH with a thermal storage system was investigated, where paraffin wax was used as a thermal storage medium, resulting in higher thermal efficiency. Karwa and Srivastava [22] presented a comparison between the thermal efficiencies of roughened and smooth duct SAH. It was found that the roughness on the airflow side of the absorber plate improved the thermal performance of SAH by 26% higher than that of a smooth duct air heater, with the highest gain found at the lowest mass flux of $0.01 \, \mathrm{kg \, s^{-1} m^{-2}}$[†].

In [23] a single pass SAH design was presented for improving the thermal efficiency of the system with increasing the solar intensity and flowrate, reaching maximum efficiencies of 40.02% and 51.50% for the flowrates 0.012 and 0.016, respectively. Paraschiv et al. [24] tested various configurations of the absorber and airflow rates through the collector. They found that thermal efficiency increased with greater airflow rate and solar radiation. The average thermal efficiencies for typical airflow rates 0.025 and 0.045 were 47% and 63%, respectively. Chabane et al. [25] experimentally investigated the effect of longitudinally arranged fins on the thermal performance of a single pass SAH. The thermal efficiency was studied at two airflow rates, 0.012 and 0.016, giving maximum efficiencies of 51.50% and 43.94%, respectively. Tyagi

---

[†] Hereafter, all units are SI unless otherwise stated.

et al. [26] experimentally evaluated the performance of a flat plate SAH subject to various flow pathways (over flow, under flow and double pass) at different airflow rates, 0.014, 0.0279 and 0.042. For a double pass flow pattern at high flowrates, a higher thermal efficiency and heat gain by air were recorded, compared with the other two flow patterns.

In [27], a new approach was introduced for SAH with conical springs placed on the absorber plate for airflow rates of 0.06 and 0.07. The maximum thermal efficiencies attained were 50.4 and 65.9%, respectively, for both Type I (without conical springs) and Type II (with conical springs). The conical springs worked as turbulators, contributing to the heat transfer enhancement for Type II compared to Type I. Ramani et al. [28] carried out experimental and theoretical studies to analyse the effect of a double pass SAH with and without porous material. The finding of this study revealed that the thermal efficiency of the system with porous media is up to 25% higher than that of the same system but without porous media, and it is up to 35% higher than that of the system using a single pass solar air collector. Further studies used an extended surface area (ribs or wavy configuration) with different arrangements positioned under the absorber for heat transfer enhancement [29, 30].

The comprehensive study of Alvarez et al. [31] was the first of its type for utilizing recycled aluminium cans (RAC). A comparison was made among six configurations of solar air systems, where the RAC showed the highest efficiency [32-36]. Filiz et al. [37] experimentally investigated the performance of a double pass solar air collector using RAC with different arrangements, namely: flat (without cans), corrugated (staggered) pattern and longitudinal. The authors found that the corrugated arrangement had the optimum performance among all collectors at 0.05 airflow rate. Based on the latter study, Hikmet et al. [38] modelled the performance of a double pass solar air collector including RAC using dimensionless methods, called 'artificial neural network' and 'wavelet neural

network' models. Their models were fairly consistent with the same findings [37]. We can conclude that the thermal efficiency of multipass solar air collectors is generally better compared to the single pass, attributed to increasing surface area without adding a valuable extra cost. In particular, the thermal performance of a single duct double pass solar air collector (U-flow shape) shows higher efficiency than other multi-pass types, specifically in hot weather countries [39].

To the best of our knowledge, only limited studies are available in literature for the impact of RAC on the SAH performance. Also, the influence of RAC with single duct double pass solar air collectors (U-flow shape) on the system performance has not been given enough attention in the past, which has motivated our study. Thus, the current study is focused on the impact of increasing turbulence in the airflow on the thermal performance of a single duct double pass solar air collector (U-flow shape). Air-flow obstacles are introduced using the RAC augmentation.

2. Methodology

Three different configurations are used in this study, namely, parallel pass double duct with a co-current flow (model A), parallel pass double duct with counter-current flow (model B), and single duct double pass U-flow (model C) (see Figure 1). The CFD model has been developed using COMSOL Multiphysics v5.3a software to examine the thermal performance of the three types of SAH. The experimental measurement is conducted for the validation of model C (the best performing configuration, based on the CFD modelling results). The flow configuration in model C is subjected to three design modifications, as shown in Figure 2, namely: SAH without RAC (i.e. plain) (model C-I), SAH with RAC in-line turbulators arrangement (model C-II) and SAH with RAC in staggered turbulator arrangement (model C-III). To evaluate pressure drop and ensure accurate results, a

comparison is made among 2D and 3D models and the empirical equations.

(a) model A

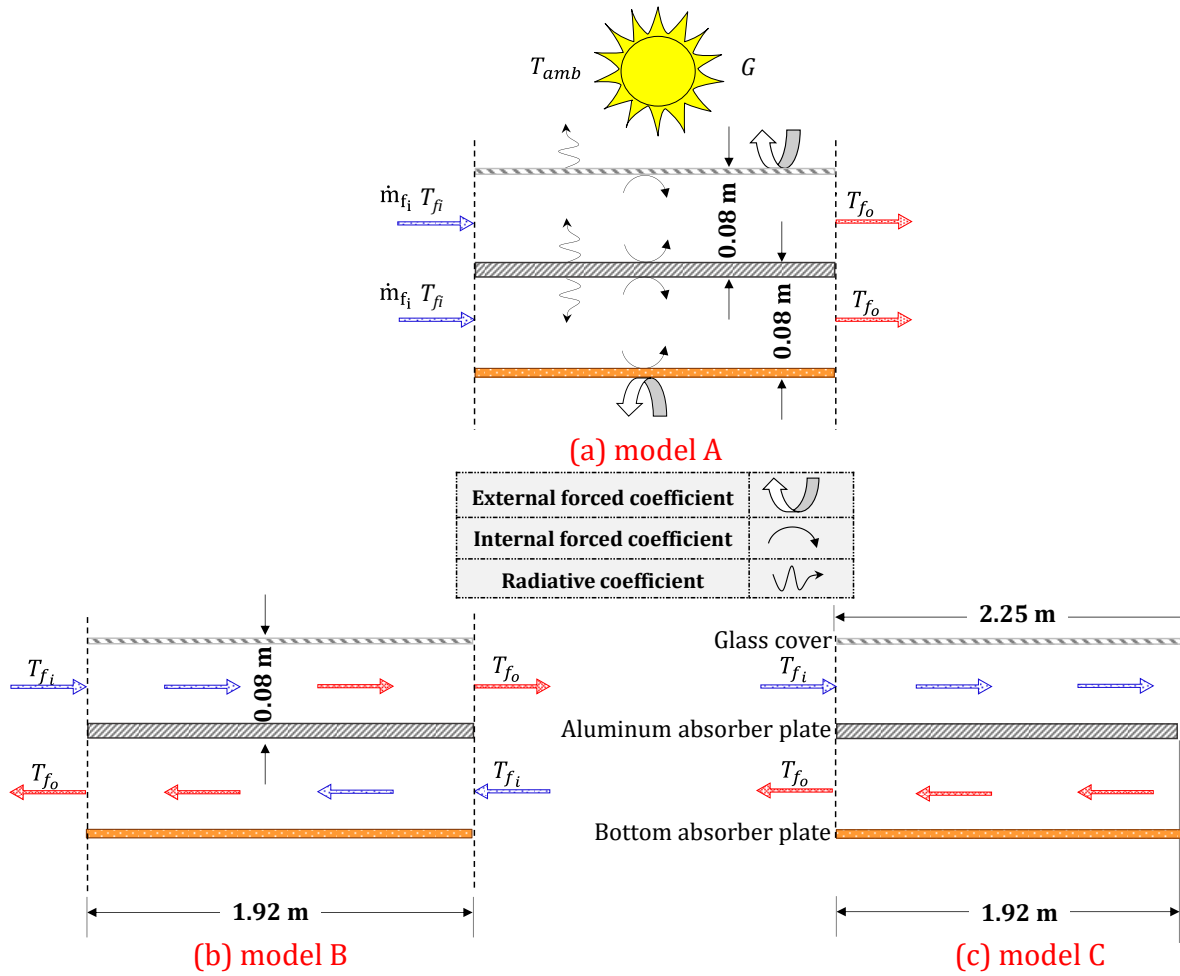| External forced coefficient	
Internal forced coefficient	
Radiative coefficient	

(b) model B

(c) model C

Figure 1. Schematics of the three solar air collectors (CFD models): (a) Cross section of parallel pass double duct of co-current flow (model A); (b) Cross section of parallel pass double duct of counter-current flow (model B); (c) Cross section of single duct double pass of U-flow (model C).
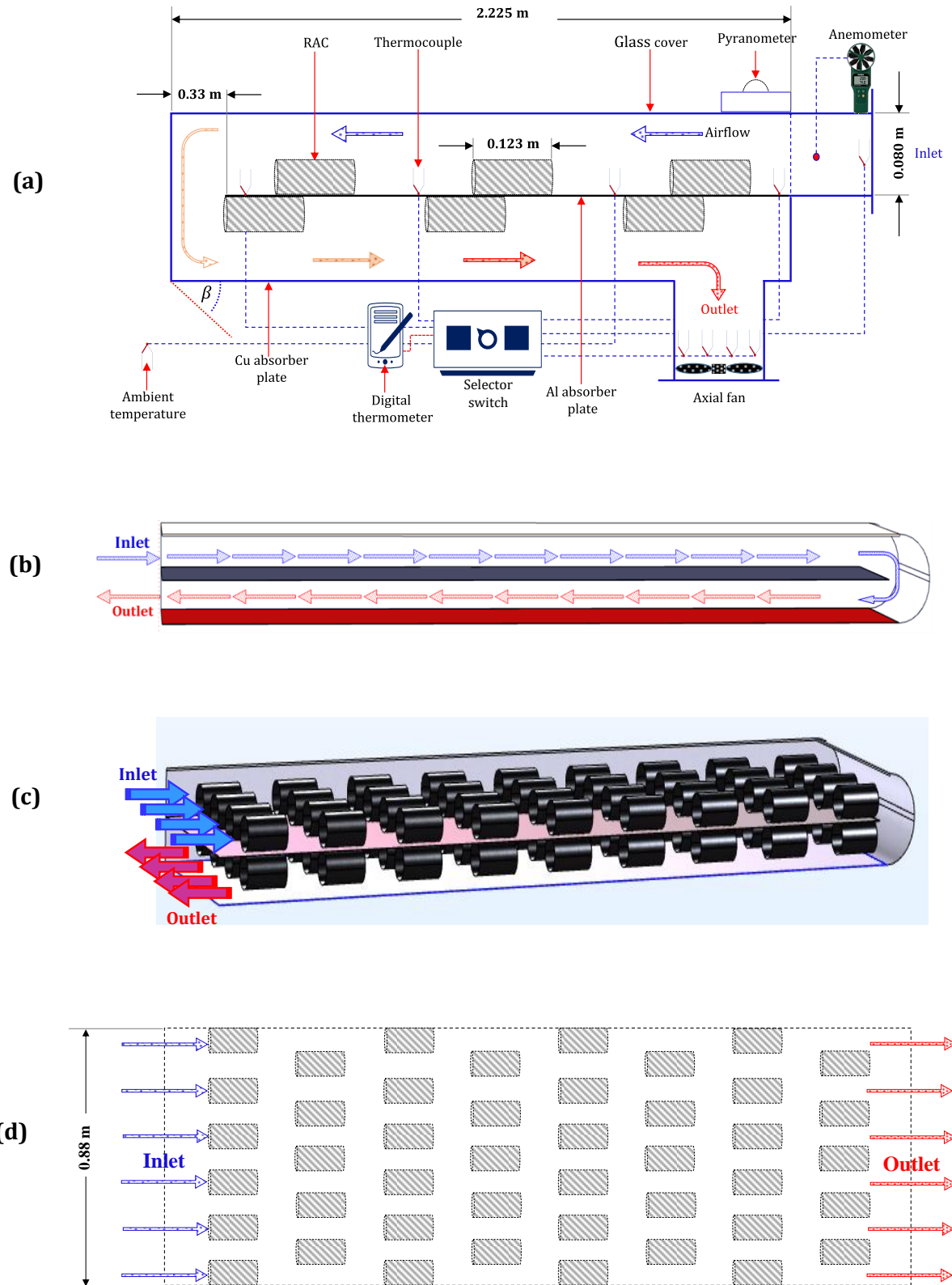
(a)

(b)

(c)

(d)

Figure 2. Schematic of single-duct double-pass (U-flow) solar air collector. (Please note that the figure is not to scale), showing: (a) The cross-section area of solar air collector including RACs; (b) SAH without RACs (model C-I); (c) Cross section of SAH with in-line pattern (model C-II).

The number of RACs is six across the width and ten along the length; and (d) Section top view of SAH with staggered configuration (model C-III). The number of RACs is seven for the first row and six for the second row across the width.

2.1. CFD modelling

2.1.1. System description

A sketch of the solar air collector designs used in this study is shown in Figure 1. The geometry comprises four main domains, namely, the solid domains of transparent glass cover, an aluminium absorber plate and the copper bottom absorber, and the fluid domain of air. The thicknesses of the transparent glass cover, aluminium absorber plate, and copper bottom absorber were 0.004 m, 0.001 m and 0.5 m, respectively, and they were all 0.82 m wide and 1.92 m long. Table 1 presents the physical properties for the material of these domains. Table 2 provides the specifications of CFD and experimental models. Three design models are proposed and investigated in this study: firstly, a parallel pass double duct (model A), where airflows over and underneath the surfaces of aluminium absorber plate in the same direction (i.e. co-current flow). Secondly, a parallel pass double duct (model B) is proposed but the flow pathways are in the opposite direction (i.e. counter-current flow). Thirdly, a U-flow model (model C) is proposed, where the airstream passes through the glass cover and the upper surface of aluminium absorber plate and reverses in the second pass through the lower surface of absorber plate and upper surface of copper bottom absorber plate (i.e. U-shape double-pass single duct flow).

Table 1. Physical properties of the CFD domains.

Layer	k	ρ	c	E
Glass	1.4	2210	730	0.84
Aluminium	238	2700	900	0.67
Copper	400	8960	385	0.65
Air	Equation (44)	Equation (42)	Equation (45)	-

Table 2. The SAH specifications for experimental and CFD models.

Collector length (m)	2.25
U-turn length (m)	0.33
Collector width (m)	0.88
Overall depth flow (m)	0.16
Upper depth flow (m)	0.80
Lower depth flow (m)	0.80
Inlet Area (m²)	0.0869
Outlet Area (m²)	0.049
width of absorber plate (m)	0.82
Length of absorber plate (m)	1.92
Exposed Area (m²)	1.57
Plate type	Flat plate

2.1.2. Conjugate heat transfer model

The relevant governing equations for the air velocity $\vec{V}(x, y, z) = u, v, w$ and temperature T are based on the conservations of mass, momentum, and energy. These are explained in subsequent sections. In order to model the coupling between heat transfer in a solid domain (i.e. the abosorber plates) and fluid flow, the conjugate heat transfer module is used in our analysis. The turbulent flow $\kappa - \varepsilon$ model is accounted for, in relevance to its compatibility with high Reynolds numbers and weakly compressible flows [40].

The Reynolds-averaged Navier-Stokes (RANS) (temporal averaging) method is applied to solve turbulent flows. These equations were solved for the conservation of momentum for two dimensional steady-state flow, which can be written as:

$$\rho\left(\bar{u}\frac{\partial\bar{u}}{\partial x} + \bar{v}\frac{\partial\bar{u}}{\partial y}\right) = F_x - \frac{\partial\bar{p}}{\partial x} + \mu\,\Delta\bar{u} - \rho\left(\frac{\partial\overline{\acute{u}\acute{u}}}{\partial x} + \frac{\partial\overline{\acute{u}\acute{v}}}{\partial y}\right), \tag{1}$$

$$\rho\left(\bar{u}\frac{\partial\bar{v}}{\partial x} + \bar{v}\frac{\partial\bar{v}}{\partial y}\right) = F_Y - \frac{\partial\bar{p}}{\partial y} + \mu\,\Delta\bar{v} - \rho\left(\frac{\partial\overline{\acute{u}\acute{v}}}{\partial x} + \frac{\partial\overline{\acute{v}\acute{v}}}{\partial y}\right), \tag{2}$$

where $\Delta\bar{u} = \frac{\partial^2\bar{u}}{\partial x^2} + \frac{\partial^2\bar{u}}{\partial y^2}$, and F_x and F_y are the external (volume) forces applied to the fluid domain. u, v and p are the momentary velocity components and pressure, respectively, $\bar{u}, \bar{v}$ and $\bar{p}$, are the time-averaged values and $\acute{u}, \acute{v}$ and $\acute{p}$ are the fluctuating velocities and pressure, respectively.

In turbulent flow, care should be taken with the flow adjacent to the wall which is different from the free stream region. In order to reduce computational time, keeping within an acceptable level of accuracy, the k-ε model is used in this study. However, this model is not accurate or valid in the vicinity of walls. Therefore, flow regions in the vicinity of walls were described using wall functions [41]. The turbulence effects were modelled using the standard two-equation κ-ε model with realizability constraints. This model included two additional transport equations and two dependent variables: the turbulent kinetic energy (κ) and the turbulent dissipation rate (ε). The turbulent viscosity was modelled as:

$$\mu_T = \rho \, C_\mu \, \frac{\kappa^2}{\varepsilon}, \tag{3}$$

where μ_T is eddy viscosity. The transport equation for κ (turbulent kinetic energy) is [42]:

$$\rho \frac{\partial \kappa}{\partial t} + \rho (u \cdot \nabla) \kappa = \nabla \cdot \left(\left(\mu + \frac{\mu_T}{\sigma_k} \right) \nabla \kappa \right) + P_\kappa - \rho \varepsilon, \tag{4}$$

u is the velocity component in the x-direction, and the production term is:

$$P_k = \mu_T \left(\nabla u : (\nabla u + (\nabla u)^T) - \frac{2}{3} (\nabla u)^2 \right) - \frac{2}{3} \rho \kappa \nabla u, \tag{5}$$

the transport equation for ε (eddy dissipation rate) [42] is:

$$\rho \frac{\partial \varepsilon}{\partial t} + \rho (V \cdot \nabla) \varepsilon = \nabla \cdot \left(\left(\mu + \frac{\mu_T}{\sigma_\varepsilon} \right) \nabla \varepsilon \right) + C_{\varepsilon 1} \frac{\varepsilon}{\kappa} P_\kappa - C_{\varepsilon 2} \, \rho \frac{\varepsilon^2}{\kappa}. \tag{6}$$

Equations (4) and (6) can be expressed in words as:

| The rate of Change of κ and/or ε | + | Transport of κ and/or ε by convection | = | Transport of κ and/or ε by diffusion | + | The rate of production of κ and/or ε | − | The rate of destruction of κ and/or ε |

In steady state condition, the two time-dependent terms disappear from Equations (4) and (6). The coefficients of the set of equations from (4) to (6) were obtained from experimental data [41]. These are $C_\mu = 0.09$, $C_{\varepsilon 1} = 1.44$, $C_{\varepsilon 2} = 1.92$, $\sigma_\kappa = 1.0$ and $\sigma_\varepsilon = 1.3$. For weakly compressible flow $\partial\rho/\partial p = 0$ and $\partial\rho/\partial\emptyset \neq 0$, where $\emptyset$ is other independent variable, such as time. The continuity equation, represented by the conservation of mass, is given in terms of time averaged incompressible flow:

$$\nabla V = 0. \tag{7}$$

The rate of heat added to the fluid particle due to heat conduction across element boundaries was the general conductive energy equation with a heat source and translational motion of the parts.

$$\frac{D(\rho c T)}{Dt} . \nabla T = \nabla.(k_s \nabla T) + \dot{Q}, \tag{8}$$

$$\nabla.(k_s \nabla T) = \frac{\partial}{\partial x}\left(k_s \frac{\partial T}{\partial x}\right) + \frac{\partial}{\partial y}\left(k_s \frac{\partial T}{\partial y}\right) + \frac{\partial}{\partial z}\left(k_s \frac{\partial T}{\partial z}\right), \tag{9}$$

$$\frac{D(\rho c T)}{Dt} = \rho c \frac{\partial T(x,y,z)}{\partial t} + \rho c u \frac{\partial T}{\partial x} + \rho c v \frac{\partial T}{\partial y} + \rho c w \frac{\partial T}{\partial z}, \tag{10}$$

ρ is the density, c is the specific heat, k is the thermal conductivity (a scalar or a tensor if the k is anisotropic). u, v and w are the velocity components in x, y and z directions, respectively, $\dot{Q}$ is the volume heat source (or sink). In a steady state condition, no internal energy conversion, two dimensions and non-moving parts are assumed, and Equation (8) reduces to be the following format (Laplace equation):

$$\nabla.(k_s \nabla T) = 0. \tag{11}$$

In the fluid domain, the following details of fluid flow behaviour are taken into account for the solution to the heat transfer:

- The energy transport is considered due to convection, in which, either the convective or conductive modes of heat transfer dominate, depending on the thermal properties.
- The viscous effects are taken into account for the production of fluid heating, which is often ignored although its impact is noticeable in viscous fluid motions.

- The compressibility effect on producing heat is considered. The pressure work term contributes to the heat equation when the fluid density becomes temperature dependent. Taking into account the abovementioned flow underlying-physics, as well as conduction, generalises the transient heat equation to the following expression [43]:

$$\rho c_{p_f} \left(\frac{\partial T}{\partial t} + V\, \nabla T(x,y,z) \right) + \nabla . \left(k_f \nabla T \right) = Q_P + Q_{vd} + \dot{Q}, \tag{12}$$

Q_{vd} is the viscous dissipation in the fluid domain, u is the velocity vector, q is the heat flux by conduction, Q_P is the work done by pressure gradients due to heating under adiabatic compression and thermo-acoustical phenomenon, which is relatively minor for a small Mach number,

$$Q_P = \alpha_p\, T \left(\frac{\partial p}{\partial t} + V.\nabla p \right), \tag{13}$$

$$\alpha_p = \frac{1}{\rho} \frac{\partial \rho}{\partial T}, \tag{14}$$

p is pressure, and for ideal gases, the thermal expansion coefficient α_p takes the simpler form:

$$\alpha_p = \frac{1}{T}. \tag{15}$$

For a steady-state problem, the temperature does not change with time and the terms with time derivatives disappear. The final governing equation is the equation of state. In reality, the density is a function for pressure and temperature,

$$\rho = \rho\,(p,T). \tag{16}$$

For ideal gas, ρ is calculated using the law of the state which is valid with Equation (42),

$$\rho = p/RT. \tag{17}$$

2.1.3. Boundary conditions

The solution domain of the 2D SAH (models A, B and C) was a rectangular duct on the x-y plane, bounded by the inlet, outlet and wall boundaries (as illustrated Figure 1). The

properties of the air, absorber plate material (aluminium) and copper absorber plates were temperature dependent based on features built into Comsol CFD software. No-slip condition (the velocity of air at a wall equal to the velocity of the wall) was assumed for the flow velocity at solid surfaces. The top wall boundary condition of the glass was subjected to U.V and I.R radiation, assuming that the glass was ultra-clear and had no absorption or emission and the insolation on the upper surface of collector is distributed uniformly across the surface [44]. The mean inlet velocity, inlet air temperature and insolation values, in comparison between model C (2D CFD model) and model C-I (experimental data), are shown in Table 3. Uniform air velocity was introduced at the inlet assuming a fully developed flow. At the exit, a pressure outlet boundary condition was specified with a fixed pressure of 101325 Pa.

According to [45] the Reynolds number was set between 10000 and 20000. In detail, the boundary conditions were as follows.

1) Along the back insulation surface, $0 \leq x \leq L$; $y = 0$,

$$u = 0, \ v = 0, (-k \ \nabla \ T_{bs}) = h \ (T_{bs} - T_{\text{amb}}), V_w = 3 \text{ m s}^{-1}. \tag{18}$$

2) Along the upper glass surface, $0 \leq x \leq L, y = \delta_{D1} + \delta_{D2}, \delta_{D1} = \delta_{D2} = 0.08$ m,

$$u = 0, \ v = 0, \ (-k \ \nabla \ T_g) = h \ (T_g - T_{\text{amb}}), \ V_w = 3 \text{ m s}^{-1}. \tag{19}$$

3) Along the upper surface of Al (aluminium) absorber plate, $0 \leq x \leq L$; $y = \delta_{D1}$,

$$u = 0, \ v = 0, \ Q = G = 1000 \text{ W m}^{-2}. \tag{20}$$

4) At the inlet of the duct:

model A: for lower inlet duct, $x = 0, 0 \leq y \leq \delta_{D1}$, while for upper inlet, $x = 0, \delta_{D1} \leq y \leq \delta_{D2}$,

$$u = \bar{u}, \ v = 0, \ T = T_{fi}, \dot{m} = \dot{m}_{fi}. \tag{21}$$

model B: for lower inlet duct, $x = L, 0 \leq y \leq \delta_{D1}$, while for upper inlet, $x = 0, \delta_{D1} \leq y \leq \delta_{D2}$.

$$u = \bar{u}, \ v = 0, \ T = T_{fi}, \ \dot{m} = \dot{m}_{fi}. \tag{22}$$

model C: for inlet duct, $x = 0, \delta_{D1} \leq y \leq \delta_{D2}$.

$$u = \bar{u}, v = 0, T = T_{fi}, \dot{m} = \dot{m}_{fi} + \dot{m}_{fi} \tag{23}$$

5) At the outlet duct: for all three models $p_{out} = 0$ (gauge pressure, or 101325 Pa absolute pressure).

Table 3. The experimental results for plain designs that are used in the validation between model C (2D CFD model) and model C-I (experimental model).

time	T_i	$\overline{V}$	G
9:00	16.9	1.26	600
10:00	20.9	0.96	671
11:00	21.9	0.96	886
12:00	24.4	1.03	996
13:00	23.9	0.99	1030
14:00	25.7	1.03	976
15:00	24.2	1.07	760
15:30	24.3	1.06	466

In order to simulate a realistic incident solar radiation, an External Radiation Source sub-node was applied to contribute to the incident radiative heat flux on the solar spectral bands (U.V, visible and I.R radiation). The surface-to-surface radiation model was used to simulate the thermal radiation exchange between all the surfaces which are governed by Equation (24), assuming that the fluid and the glass cover were non-participating, i.e., they do not absorb, emit, or scatter any radiation. This is valid since the glass cover is ultra-clear and the thickness is less than 6 mm [46].

$$q_r = \varepsilon\,(G - E_b) = \varepsilon\,\sigma\,(T_s{}^4 - T^4). \tag{24}$$

$$E_b = \sigma\,A_s\,T_s{}^4. \tag{25}$$

Forced convective boundary conditions were applied to the top surface of the glass cover and the bottom surface of collector insulation. The average wind velocity value was assumed as 2.7 m s^{-1} (see Figure 3) based upon observation data agreeing with [47, 48]. To estimate the forced convective heat transfer coefficients for these two surfaces, the following empirical correlations are used [46]:

$$h_{f(g-\text{amb})} = \frac{2\,k}{L}\,\frac{0.3387\,\text{Pr}^{1/3}\,\text{Re}_L{}^{1/2}}{\left(1 + \left(\frac{0.0468}{\text{Pr}}\right)^{2/3}\right)^{1/4}}\ \{\text{for Re}_L \leq 5 \times 10^5\}, \tag{26}$$

$$h_{f(g-\text{amb})} = \frac{2\,k}{L}\,\text{Pr}^{1/3}\left(0.037\ \text{Re}_L{}^{4/5} - 871\right)\{\text{for Re}_L > 5 \times 10^5\}, \tag{27}$$

where $Re_L = \frac{V_w L_c}{\upsilon}$ is a function of the characteristic length (L_c), which is equal to the length of

the collector (L) in case of inclined collector. In the case of horizontal mounting, $L_c = \frac{A_s}{Pe}$, V_w is the

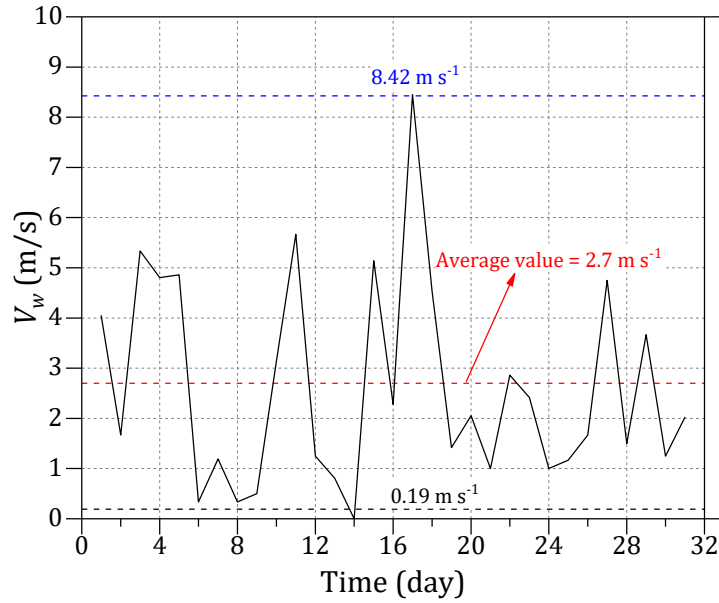average wind velocity, and υ is the kinematic viscosity.

Figure 3. The wind data observation for March in Ramadi city, Iraq.

2.1.4. Mesh independence study

Generally, computational domains could be meshed using structured (quad element

type), unstructured (i.e. Triangular element type), or hybrid (i.e. combination of

unstructured and structured) elements. The choice of mesh element type depends on the

physical characteristics (e.g. turbulent or laminar flows), and the geometry of the

problem (e.g. curved or straight). The examination of the impacts of mesh type and

density on the solution accuracy, computational efficiency, and stability are investigated.

Three independent mesh tests were carried out for model C (see Table 4), starting from

very coarse to extremely fine element sizes. The interface between solid and fluid

domains (thermal and hydrodynamic boundary layers) and the U-turn region (i.e. the

region when the air flows from upper channel to lower channel) were discretised for a

fine mesh adjustment as shown in Figure 4.

Table 4. Structured mesh independent test analysis (free quad elements) for model C, using the boundary conditions $U_m = 2.254$ m s^{-1}, Re=20000, G=1000 W m^{-2} and T_i =35 °C.

| Trial No	Refinement step	No of Elements	Time (s)	RAM (GB)	η_{th}	Δp (Pa)	MEQ	RT
1	Extremely coarse (quad)	880	27	1.63	50.156	8.3516	1	0.001
2	Very coarse (quad)	2024	24	1.83	51.927	10.14	1	0.001
3	less coarse (quad)	4110	38	1.96	52.116	10.39	1	0.001
4	Coarse (quad)	6764	61	2.22	52.203	10.355	1	0.001
5	Normal (quad)	13150	141	2.69	52.252	10.336	1	0.001
6	Fine (quad)	22440	250	3.33	52.238	10.339	1	0.001
7	Very Fine (quad)	35948	473	3.86	52.243	10.335	1	0.001
8	Extremely fine (quad)	112770	2907	7.07	52.271	10.344	1	0.001
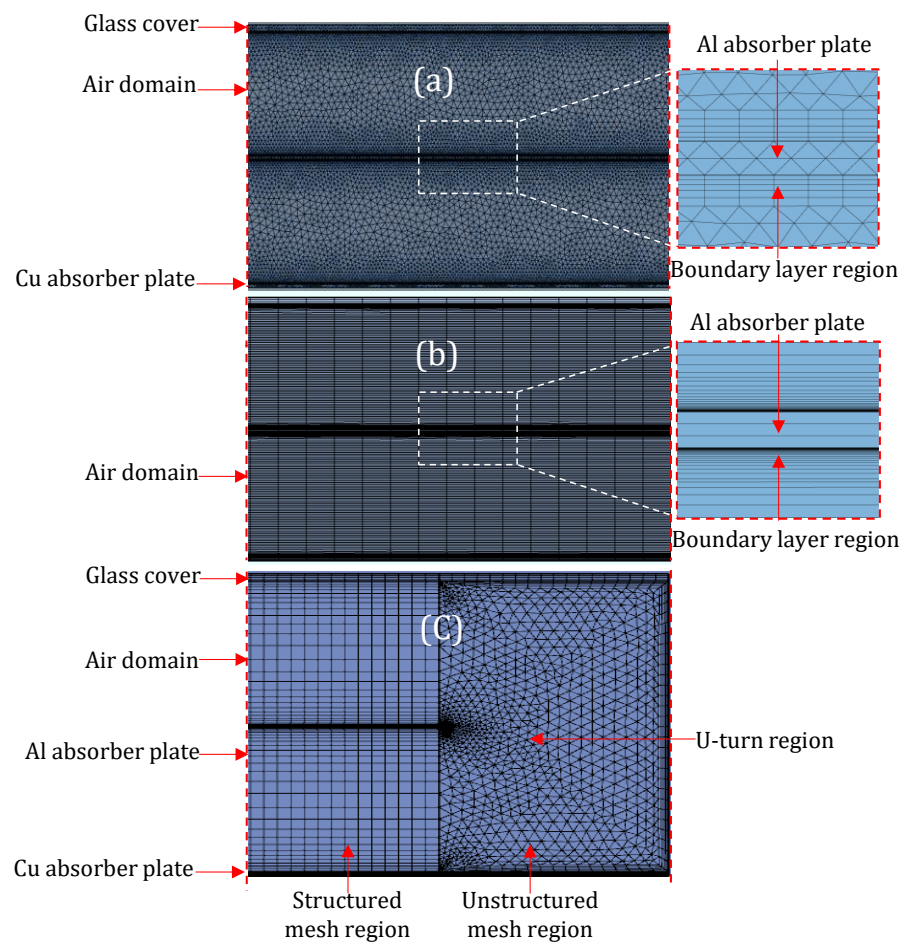
Figure 4. System meshing, using (a) unstructured, (b) structured, and (c) hybrid meshes.

The third mesh provided segmentation of the system into two regions by using free triangular elements for U-turn region and free quad elements for the other regions where the mesh could be more compatible in terms of shape of geometry.

Table 5. Unstructured mesh independent test analysis (free triangular elements) for model C, using the boundary conditions $U_m = 2.254$ m s^{-1}, Re=20000, G=1000 W m^{-2} and $T_i =35$ °C.

Trial No	Refinement step	No of elements	Time (s)	RAM (GB)	η_{th}	Δp (Pa)	MEQ	RT
1	Extremely coarse (Triangular)	17011	325	1.76	55.593	9.5503	0.4432	0.001
2	Very coarse (Triangular)	33649	401	3.4	55.946	10.159	0.2183	0.001
3	less coarse (Triangular)	41943	534	3.96	55.96	10.279	0.204	0.001
4	Coarse (Triangular)	45388	845	4.05	55.929	10.26	0.1961	0.001
5	Normal (Triangular)	48756	976	4.1	55.923	10.352	0.1795	0.001
6	Fine (Triangular)	58256	796	4.2	55.907	10.362	0.1853	0.001
7	Very Fine (Triangular)	105094	2870	5.51	55.929	10.436	0.175	0.001
8	Extremely fine (Triangular)	264432	21888	13	55.891	10.439	0.1773	0.001
Hybrid	Fine	77484	1481	2.82	55.873	10.24	0.1624	0.001

As can been seen from Tables 4 and 5, the minimum element quality (MEQ) of structured mesh was much higher than that of the unstructured mesh, while the RAM (random access memory) computational time and the number of elements were significantly reduced using the structured mesh. Thus, this test has actively contributed to reducing the running time and RAM, respectively, from 976 sec and 4.1 GB (using unstructured mesh) to 141 sec and 2.69 GB (using structured mesh).

2.2. Experimental Setup

The experimental set up was designed to be tested outdoors for data collection. The flow pattern selected was a single duct double pass (U-flow). The RACs were installed on the top and bottom of the absorber plate in front of the airflow, which was completely open

from two sides for direct exposure to airflow. The schematic illustration of the double-flow SAH set up is shown in Figure 2 (a, b, c and d). In this study, three types of absorber plates were used in order to compare the thermal performance of SAH with and without RAC, namely, SAH without RAC (model C-I), SAH with RAC in the in-line pattern (model C-II) and SAH with RAC in a staggered pattern (model C-III).

2.2.1 Geometry and design considerations

The dimensions of the Al and copper (Cu) absorber plates were 1.92 m long, 0.82 m wide and 0.001m in thickness. A single glass sheet of 4 mm thickness was fixed above the Al absorber plate as a transparent glass cover, with a gap (depth flow) of 0.08 m. This solar air collector consisted of two passes; the airflow in the first pass (between the glass cover and the Al absorber plate) and the airflow reverses in the second pass (between the two absorber plates) to form a U-shape flow. The copper absorber plate was positioned on the bottom duct. All material properties and the specifications of these collectors are shown in Table 1 and Table 2. The ambient air was supplied by a low-pressure axial fan with a maximum power of 18 W, which was placed at the outlet of the collectors. The RAC capacity is 330 ml, with 0.123 m in length and 54 mm diameter.

In achieving a feasible, affordable and optimal design of the solar air collector, different considerations were taken into account.

- The frame of the channel duct was fabricated from a compact wood panel (0.02 m thickness) instead of using galvanized steel that should cover with glass wool insulation or other type insulation. This potentially reduced the weight and cost of the collector, decreased the edge heat transfer losses and allowed flexibility to install instrumentations such as thermocouples.

- In order to maximize the incident solar radiation, the maximum tilt angle ($\beta = 27°$ [48]) was considered for this study and the solar collectors were facing the south [49].

- To ensure perfect contact between the RAC and Al absorber plate, two metallic washers bolted with screw were placed on the contact area between the RAC and Al absorber plate.

- In order to set the system as close as to the real conditions, the effect of entrance length was neglected. This is because of the difficulty in the installation, operating and architectural or structural requirements. Also, from the hydrodynamic and thermodynamic boundary layer point of views, the convective heat transfer coefficient in the developing region is higher than the developed ones [50].

- In order to ensure that the flow is entering in a turbulent state, the depth of flow (δ_D) was selected according to the optimization criterion at different flowrates, suggested by [45] [51] as presented in Equation (28). $\mathcal{L}$ is the airflow path length from inlet to outlet, and thus, $\mathcal{L} = 2L$ for model C-I and model C (U-flow shape) and $\mathcal{L} = L$ for other models, in the range:

$$(\mathcal{L}/D_h)_{\text{optimum}} \geq 30. \tag{28}$$

- In order to improve the absorption and emissions, and to reduce the reflectivity (optical features) for the absorber surfaces, the Al and Cu absorber plates and RAC were roughened. This was made using coarse sandpaper measuring 40 to 60 grit and painted with black chrome nonselective coating for affordability and availability in the market.

- In order to mount the collector, a base frame is made of aluminium to carry the collector and change the tilt angle for matching the maximum incident solar radiation.

2.2.2 Instrumentation and measurements uncertainty

For each collector, ten *K*-type thermocouple sensors were used; four of them were distributed equally along the flow direction on the top surface of the aluminium absorber plate. Five well-insulated thermocouples were installed at the inlet and the outlet collectors, one in the inlet and the rest in the outlet. Also, the air ambient temperature was measured in the shaded area using ventilated wooden Stevenson screens criteria [52], above the ground 1.5 m and behind the collector. All sensors were connected to a digital thermometer (as shown in Figure 2). The thermocouples were calibrated with an average error of 1.1 °C. The inlet air velocity was measured by using a multifunctional anemometer device a Testo Vane Anemometer with an uncertainty of ±2%. The measurement range of the anemometer is 0.5-25 m s^{-1} with a resolution of 0.1 m s^{-1} [53].

An accurate and reliable solar meter type CMP3 pyrometer was used to measure the incident solar radiation [54]. The capability of this tracker is to measure direct, diffused and

global radiation with a resolution of 0.5 Wm-2. This meter was installed parallel to the collector, and the values were validated with estimated values in [51] with a high level of conformity (PPMCC = 0.95 and RMSE =9.32) as shown in Figure 5. Care was taken to avoid the accumulation of dirt on top of the glass surface, with regular cleaning.
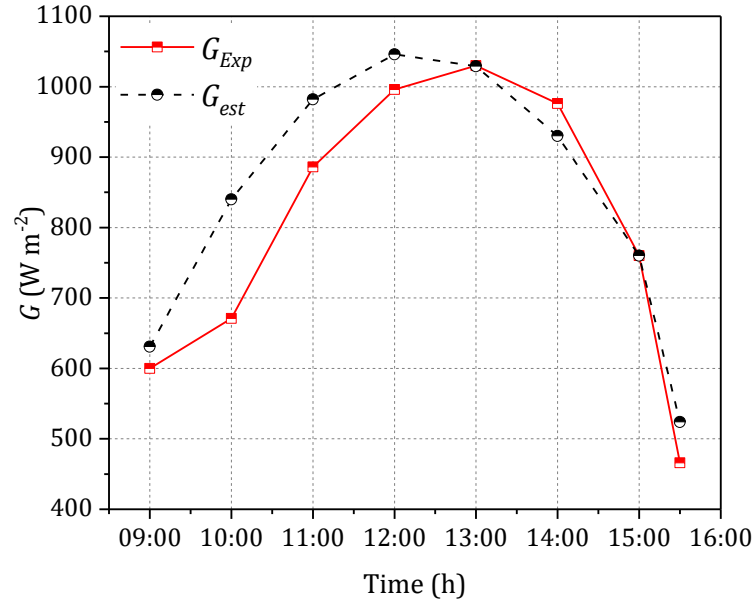

Figure 5. Intensity of solar radiation (G) versus time recorded in 23 February, showing the experimental [54] and estimated [51] data.

2.3. Thermo-hydraulic performance

The heat benefit delivered by the solar air collector is estimated as:

$$\dot{Q}_u = \dot{m} c_p (T_o - T_i), \tag{29}$$

where $\dot{m}$ is the mass flowrate,

$$\dot{m} = \rho \, \bar{V} \, A_c, \tag{30}$$

ρ is the density of air, $\bar{V}$ is the mean velocity at the inlet boundary air conditions, and A_c is the channel ducting cross section area. The total heat generated by solar irradiation (total incident solar radiation) is given as:

$$\dot{Q}_s = G \, A_s, \tag{31}$$

G is the incident solar radiation and A_s is the surface (aperture or exposed) area.

The conventional method in evaluating the net thermal energy output of the solar collectors is calculated by subtracting theoretical fan power or pump power consumption (see Equation (34)) from the thermal output. In reality, the fan power required to drive the air in solar air collectors are affected by many factors and this method does not consider that the part of the energy will be lost and consumed in conversion and transmission losses. These losses are attributed to the efficiency of fan or blower η_f = 0.65, the efficiency of the electric motor used for driving fan is η_m = 0.88, the efficiency of electrical transmission from a power plant is η_{tr} = 0.92, the thermal conversion efficiency of power plant is η_{thc} = 0.35. It is appropriate to combine these coefficients into one named conversion factor (C_f), which accounts for the overall efficiency of energy conversion from thermal energy to mechanical energy[55],

$$C_f = \eta_f\, \eta_{tr}\, \eta_m\, \eta_{thc} = 0.18. \tag{32}$$

In order to represent realistic conditions in solar air collectors, the effective thermal efficiency η_{th} is accounted for together with C_f,

$$\eta_{th} = \frac{\dot{Q}_u - (P_f/C_f)}{\dot{Q}_s}. \tag{33}$$

The instantaneous fan power required of a particular collector model could be estimated by

$$P_f = \Delta p\, \dot{V}, \tag{34}$$

where Δp is the total pressure drop experienced by the air stream in passing through a channel at a flowrate $\dot{V}$ due to flow friction and losses at the channel entrance, exit and various fittings, expressed as:

$$\Delta p = \Delta p_f + \Delta p_{\text{other}}, \tag{35}$$

the pressure drop owing to friction (Δp_f) is given as:

$$\Delta p_f = \frac{\rho\, f V^2\, L}{2\, D_h}, \tag{36}$$

ρ is the density of air, f is the Fanning friction factor for turbulent flow calculated by [56],

$$f = 0.079 \, \text{Re}_D{}^{-0.25} \quad \{\text{for } 6000 < \text{Re}_D < 100000\}. \tag{37}$$

The Fanning friction factor for laminar flow estimated as [57]:

$$f = \frac{g_f}{\text{Re}_D} \quad \{\text{for } \text{Re}_D < 2300\}, \tag{38}$$

where g_f is the geometry factor which changes depending on the geometry type (see the criteria in [57]), $\text{Re}_D = \frac{\bar{V} \, D_h}{v}$ is the Reynolds number, the ratio of the inertial forces and the viscous forces, $\bar{V}$ is the mean velocity of air at inlet temperature (T_i), and D_h is the equivalent diameter for channel duct at the inlet diameter $D_h = 4 \, A_c / pe$.

Other pressure drop values (minor losses) as a result of the effects of channel entrance, exit, elbows, bends, joints, and valves are determined by the formula:

$$\Delta p_{\text{other}} = \left(\frac{1}{2}\right) k_L \, \rho \, \bar{V}^2, \tag{39}$$

$$k_L = k_{\text{entance}} + k_{\text{exit}} + k_{\text{bend}}, \tag{40}$$

the coefficients k_{entance} and k_{exit} are set to the values 0.5 and 1.0 for the entrance and exit losses, respectively. In the case of close return bend inside this collector, k_{bend} value was taken equal to 2.2, [58] [59]. For the sake of accuracy, the entrance and exit coefficients (minor losses) were excluded from the calculation of pressure drop when comparing between the CFD models and empirical correlations. The air properties were evaluated at the mean fluid temperature. The air properties can be calculated by using the following correlations at inlet air temperature [40], verified against those presented in [60]:

$$\mu = -8.39 \, e^{-7} + 8.36 \, e^{-8} \, T_i - 7.695 \, e^{-11} \, T_i{}^2 + 4.65 e^{-14} \, T_i{}^3 - 1.07 \, e^{-17} \, T_i{}^4, \tag{41}$$

$$\rho = 3.9147 - 0.016082 \, T_i + 2.9013 e^{-5} \, T_i{}^2 - 1.9407 e^{-8} \, T_i{}^3, \tag{42}$$

$$v = \frac{\mu}{\rho}, \tag{43}$$

$$k = -0.0023 + 1.155 \, e^{-4} \, T_i - 7.91 e^{-8} \, T_i{}^2 + 4.118 e^{-11} \, T_i{}^3 - 7.44 e^{-15} \, T_i{}^4, \tag{44}$$

$$c_p = 1047.7 - 0.373 \, T_i + 9.46 e^{-4} \, T_i{}^2 - 6.03 e^{-7} \, T_i{}^3 + 1.29 e^{-10} \, T_i{}^4. \tag{45}$$

3. Results and discussion

3.1 Thermal performance examination of U-flow shape design

The three models show that the double pass single duct solar air collector has a higher efficiency than other types of flow arrangements (see Figure 6).
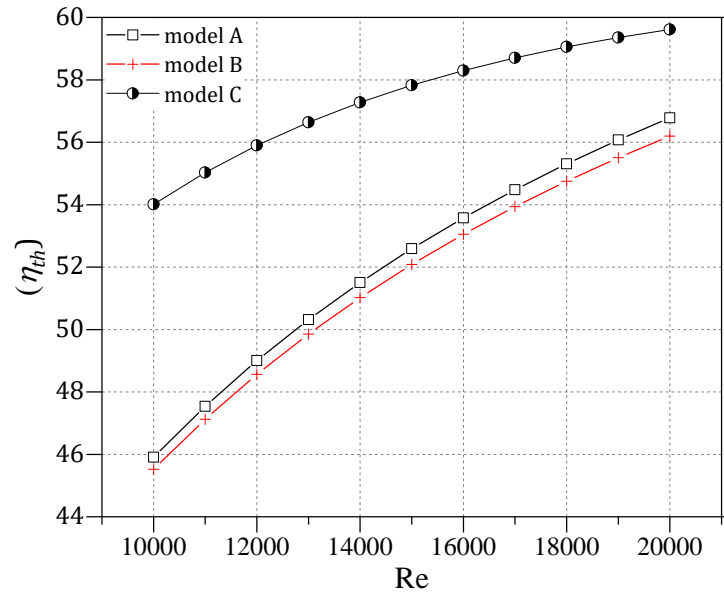

Figure 6. The thermal efficiency versus Reynold number under turbulent condition regime for co-current flow (model A), counter-current flow (model B) and U-flow (model C) CFD models.

In Figure 6, the average thermal efficiencies are presented for three models, namely: parallel pass double duct (co-current), parallel pass double duct (counter-current flow), and single duct double pass (U-flow) for the flow range $10000 \leq \text{Re}_D \leq 20000$. As can be seen from this figure, the average thermal effective efficiency of the U-flow model is the highest (up to 57.42 %), compared to the co-current (up to 52.1%) and counter-current (up to 51.6%) efficiencies, for the tested flow range ($10^3 \leq \text{Re}_D \leq 2 \times 10^3$). This is owing to the length of air path being longer than other models which in turn leads to accumulation of heat along the flow path increasing the outlet air temperature. It should be emphasised that improving the thermal efficiency of a certain model is made on the expense of power fan effectiveness. For instance, the U-flow model requires a fan power of about 15.7 times more than that consumed for the other two models. The average power fan consumption of models A and B is 0.364 W, each, while for model C is 6.097 W. The numerical

values of pressure drop for the three models are illustrated in Figure 7. In this figure there is a marked increase in pressure drop for U-flow model (model C) compared to the other two models. This is due to the induced flow separation in the U-turn near the bend and the swirling secondary flow that occurs because of the imbalance of centripetal forces as a result of the curvature of the duct centreline. The U-flow model (C), however, offers the highest efficiency compared to the other two models (A and B).
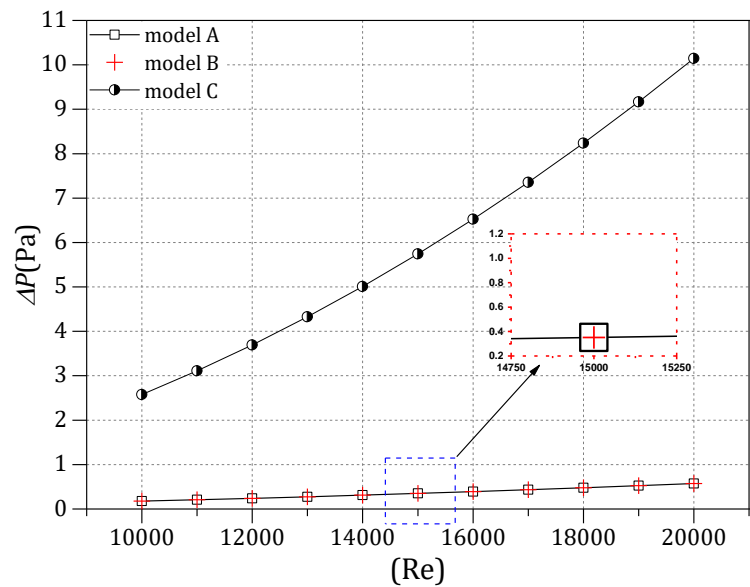
Figure 7. The pressure drop in flow duct between the inlet and the outlet for (co-current flow, model A), (counter-current flow, model B) and (U-flow, model C) CFD models.

3.2. Experimental results

The experiments were conducted in Ar-Ramadi City, Al-Anbar province – the western region of Iraq (longitude: 33.25°N; latitude: 43.18°E) under clear sky conditions on 23rd February (model C-I) and 27th February (model C-II) and 2nd March (model C-III) between 09:00hr and 15:30hr. The average mass flow rates were 0.096 for model C-I, 0.088 for model C-II, and 0.0819 for model C-III. The solar radiation versus time for the three different dates are measured using solar tracker device [54], and presented in Figure 8. The average hourly values for the measured insolation against time during January–August are verified using data in [48] and presented in Figure 9.
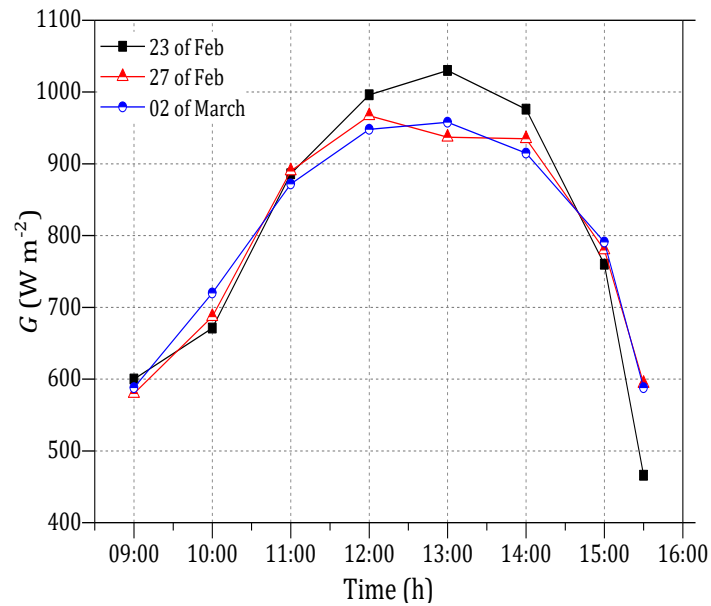
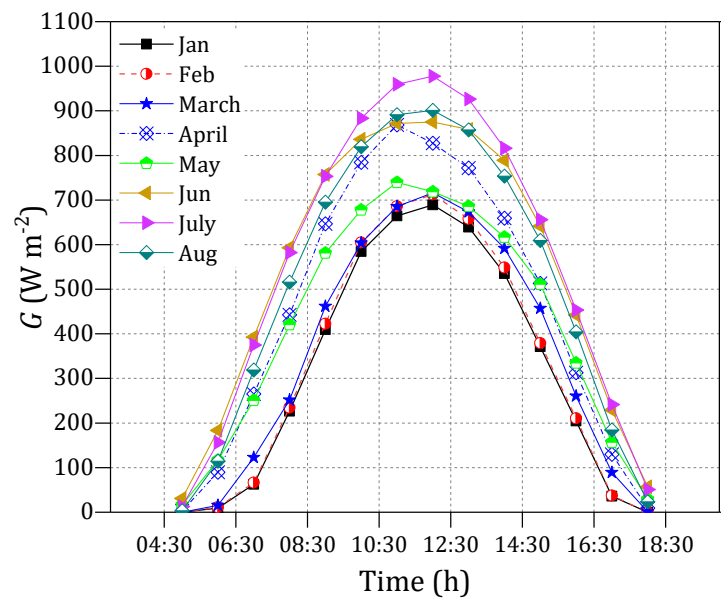Figure 8. Intensity of solar radiation versus time recorded on three different dates.

Figure 9. Intensity of solar radiation versus 4:30 to 18:30 hours recorded during January–August.

In Figure 9, the intensity of solar radiation in July was the highest; while in January, it was the lowest. Also, the solar intensity increases gradually from sunrise to reach a peak value at the solar noon (12:00hr) and it reduces until sunset. However, the values of insolation were higher than the average values for the whole month. For example, the insolation values of three days at 12:00hr (see Figure 8) were in the range 950– 1000 W

m^{-2}; while the average insolation for the whole month was less than 700 W m^{-2}. This is due to the three data values being taken on a slope collector angle (β) of 27° for that specific day; while the solar tracker device was measured on a horizontal surface [54]. This difference can also be attributed to the fact that fluctuation of weather conditions is affected by several factors, such as dust and cloud. It should be emphasised that the three tested models were exposed to almost the same weather conditions.

Figures 10 presents the influence of ambient temperature and incident solar radiation on the outlet air temperature for three models: (a) Single duct double pass (solar air collector without cans) (model C-I); (b) Single duct double pass (solar air collector with in-line cans arrangement) (model C-II); and (c) Single duct double pass (solar air collector with staggered cans arrangement) (model C-III). The trends in this figure revealed that the outlet temperature generally followed the ambient temperature and incident solar radiation closely. At certain times, however, the outlet temperature acted independently from the incident solar radiation or inlet temperature. For instance, in Figure 10a, the outlet temperature slightly increased despite a dramatic decrease in the incident solar radiation value. This is because the ambient temperature at 15:30hr remained constant and was dominant relative to the low and decreasing solar radiation intensity.

The experimentally measured thermal efficiencies of the three different models (model C-I, model C-II and model C-III) versus time are presented in Figure 11. It is found that the efficiency increased with increasing contact surface area (i.e. using RACs). The results show that the average thermal efficiencies of the staggered, in-line, and plain models are 60.2%, 53.1% , and 49.4%, respectively. The staggered arrangement offers secondary flow development which has enhanced its thermal efficiency. In contrast to the latter effect, less vortices were found in the less efficient in-line configuration although the number of RAC and the mass flowrate were higher than those of the staggered arrangement. No vortices were generated in the plain model; hence, the lowest thermal efficiency.
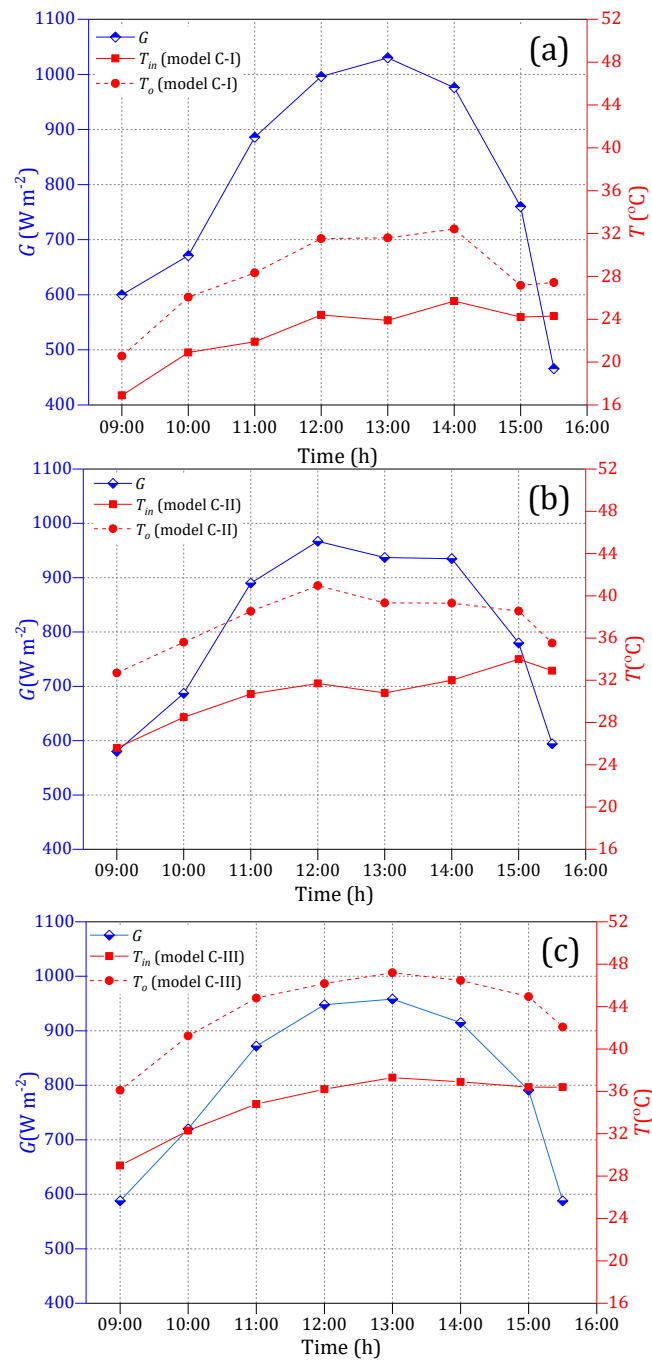
Figure 10. Collector air temperatures and incident solar radiation versus 09:00–16:00 hrs for the three models, C-I (a), C-II (b), and C-III (c).
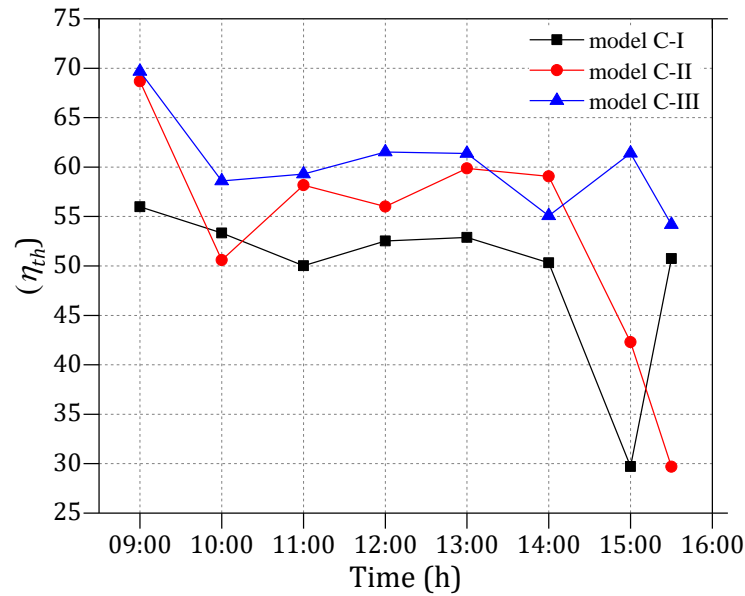
Figure 11. Thermal efficiencies versus 09:00–16:00 hrs for three configurations, model C-I (plain), model C-II (in-line) and model C-III (staggered).

Figure 12 presents the thermal efficiency, inlet air temperature, inlet velocity and intensity solar radiation values versus time for a double duct one pass solar air collector with staggered RAC design (model C-III). The thermal performance of model C-III is the best among the other two models. The thermal efficiency is dependent on the incident solar radiation and inlet air temperature throughout the day. The figure shows independent behaviour at 10:00hr, when the thermal efficiency decreased with increasing irradiation and inlet air temperature. This is attributed to the sudden drop in inlet air velocity which affected the thermal efficiency more than the other two parameters. Additionally, the inlet air velocity at 10:00hr was the lowest during the day.
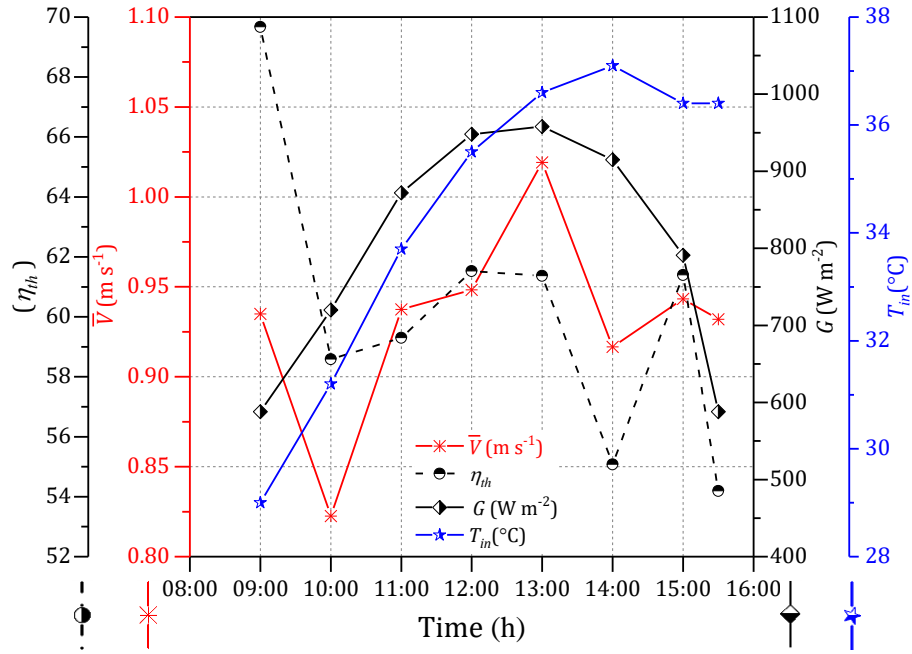
Figure 12. Thermal efficiency, intensity of solar radiation, inlet air temperature, and inlet air velocity versus 09:00–16:00 hrs for model C-III (staggered arrangement).

The daily average air temperature difference δT_{air}, aluminium absorber plate temperature T_p and collector thermal efficiency η_{th} are presented in Table 6. The maximum δT_{air}, T_p and η_{th} are seen for the staggered model (model C-III). A higher air temperature difference of 8.68°C is achieved using the staggered model, compared to 7.24°C and 5.60°C for heaters with RACs arranged in the in-line pattern and Plain plate heater, respectively. The average absorber plate temperatures are 47°C, 43.73°C and 40.94°C for the RAC staggered, in-line and plain heater configurations, respectively. Also, as can be seen from this table, the thermal efficiency of SAH with RAC arranged in staggered pattern is about 60.2% which is the highest among those used this study.

Table 6. The daily average of δT_{air}, T_p and η_{th}.

Model	δT_{air} (°C)	η_{th}	T_p (°C)	Re$_D$
C-I	5.3	49.4	40.9	9970
C-II	7.1	53.1	43.7	9009
C-III	8.45	60.2	47.1	8290

3.3. Comparison between numerical and experimental results

Statistical analysis was performed to quantify the level of conformity between the numerical (X_i) and experimental results (Y_i) of the double pass solar air heater (model C-I). The root-mean-square error (RMSE) and the Pearson product-moment correlation coefficient (linear correlation) (PPMCC) [61] were evaluated for this analysis. The RMSE can be written in the following expression:

$$\text{RMSE} = \sqrt{\frac{\sum_{i=1}^{N}(e_i)^2}{N}}, \tag{46}$$

where $e_i = \frac{X_i - Y_i}{X_i} \times 100$, and the PPMCC is expressed as:

$$\text{PPMCC} = \frac{N\left(\sum_{i=1}^{N} X_i\, Y_i\right) - \left(\sum_{i=1}^{N} X_i\, Y_i\right)}{\sqrt{N\sum_{i=1}^{N}(Y_i)^2 - \left(\sum_{i=1}^{N} Y_i\right)^2} \cdot \sqrt{N\sum_{i=1}^{N}(X_i)^2 - \left(\sum_{i=1}^{N} X_i\right)^2}}, \tag{47}$$

N is the number of data.

The hourly distribution of numerical and experimental results of the outlet air and the bulk fluid temperatures are displayed in Figure 13 for model C-I on 23rd Feb. The average, maximum and minimum percentage error were 11.6%, 16.9% and 7.3%, respectively, which can be considered to be acceptable range values [62, 63]. The RMSE and PPMCC for outlet air temperature were 13.74 and 0.98, respectively. Whilst these were PPMCC = 0.98 and RMSE = 13.74 for the bulk fluid temperature. Such a noticeable deviation between experimental and numerical results can be attributed to the following factors:

- The accuracy in measuring the wind velocity, insolation and ambient temperature.

- Dust accumulation.

- The difficulty in estimating the roughness of the absorber and channel surfaces.

- The accuracy in estimation of the optical properties such as the emissivity of the absorber plates.

- The CFD model is simplified to a two-dimensional problem whereas the physical system is three dimensional.

- Measurement uncertainty of devices.

- Despite the solar collector systems governing to quasi-steady conditions [64], in reality, the system is inherently time-dependent.

- Experimentally measured values of turbulence quantities at the inlet boundary are also required for accurate CFD simulation for turbulent flow. In the case of the $\kappa - \varepsilon$ turbulence model, turbulent kinetic energy κ and turbulent dissipation rate ε are required. When these values are not available from experimental data, they must be predicted using the following set of equations [65].

$$\kappa = \frac{3}{2}(\bar{V}_{\text{ref}} \, TI)^2 \tag{48}$$

$$\varepsilon = C_\mu{}^{3/4} \frac{k^{3/2}}{l} \tag{49}$$

$$l = 0.07L \tag{50}$$

where $\bar{V}_{\text{ref}}$ is the mean reference stream velocity, TI is turbulence intensity, l is the turbulence length scale, and C_μ is the $\kappa - \varepsilon$ turbulence model constant.

- To explain the variation between experimental and numerical mean fluid temperature, the method used in estimating the experimental mean fluid temperature was arithmetic, $\bar{T}_f = (T_i + T_o/2)$ which is less accurate compared to the integration method used in CFD modelling. Moreover, the thermocouples used for measuring the air flow temperature are only installed at the inlet and outlet collectors, which is not along the air flow direction.
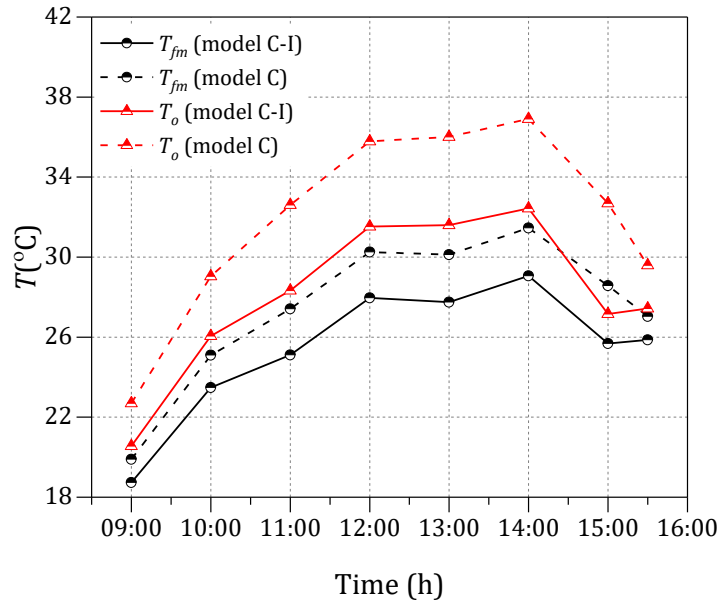

Figure 13. The inlet and outlet air temperatures versus 09:00–16:00 hrs of the experimental (model C-I) and CFD (model C) results of the plain design.

Figure 14 presents a comparison between the experimental (model C-I) and simulation (model C) temperatures of the absorber plate. The deviation PPMCC = 0.85 and RMSE =9.1 of mean plate temperature $\bar{T}_p$ was less than those seen in the measurements of fluid temperatures $\bar{T}_f$ and T_0. This is due to the fact that the number of thermocouples fixed along the absorber plate were higher than the only two thermocouples placed at the inlet and outlet.
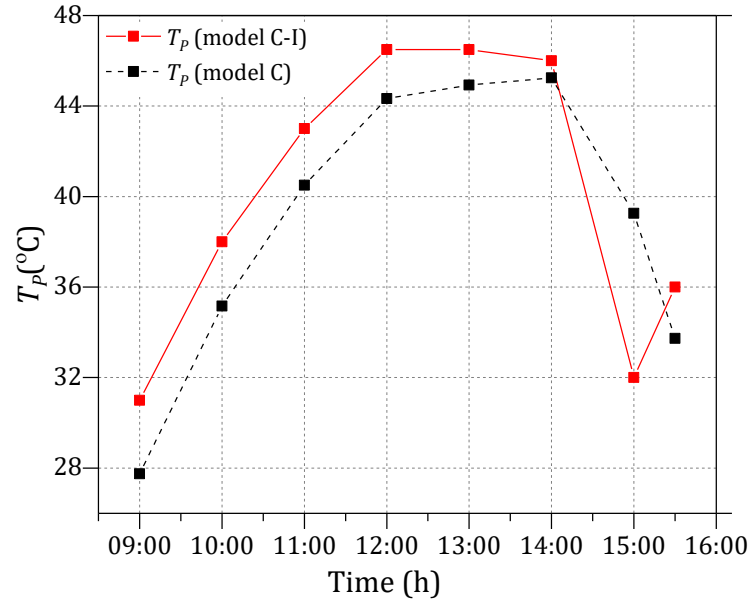

Figure 14. The absorber Aluminium plate temperatures versus 09:00–16:00 hrs of the experimental (model C-I) and CFD (model C) results of the plain design.

3.4. Pressure drop evaluation

Estimating accurate pressure drop is crucial for the design and performance of the system [66] . Accordingly, a comparison was made between empirical equations (i.e. the set of equations from (34) to (40)) and CFD results for 2D (see Figure 15a) and for 3D (see Figure 15b) cases. The comparison among CFD (2D and 3D cases) and experimental results are shown in Figure 15. As can be seen from Figure 15 and Figure 16, the highest pressure-drop was for the 3D model followed by the 2D model, with the lowest found for the empirical data. This is due to:

- The 3D model being more representative of real-life conditions than the 2D model.

- More parameters being considered in the 3D model than those in the empirical correlations, such as the wall friction (i.e. turbulent model), boundary layer separation in curved (U-turn) region and the effect of entry length before becoming the flow fully developed.

- The empirical equations results being based on fully developed condition unlike the other two models (i.e. 2D and 3D models)[67, 68].

Additionally, the empirical correlation is subject to $\mp$ 25% uncertainty which is valid with work made by Manglik and Bergles [69]. Table 7 compares among 2D CFD, 3D CFD and empirical data for the pressure drop estimated for design model C-I. The percentage errors, E, were estimated regarding the solutions from 3D-CFD. The percentage errors of empirical equations results E_1 and the percentage error for 2D-CFD is E_2.
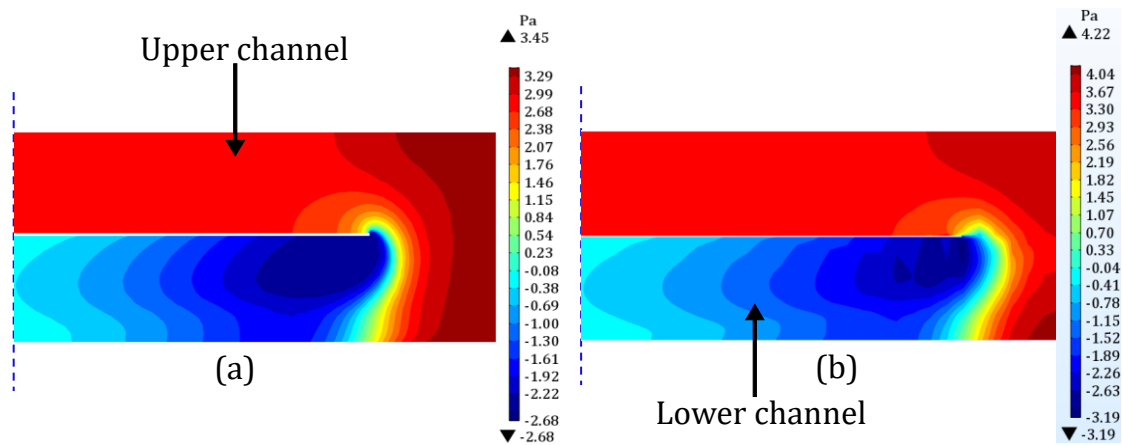

Figure 15. The pressure drop profile for model C-I (single duct double pass U-flow design without cans) with $U_m = 1.262$ m s^{-1}, $G = 600$ W m^{-2} and $T_i = 16.9$ °C conditions; (a) 2D CFD model and (b) 3D CFD model.
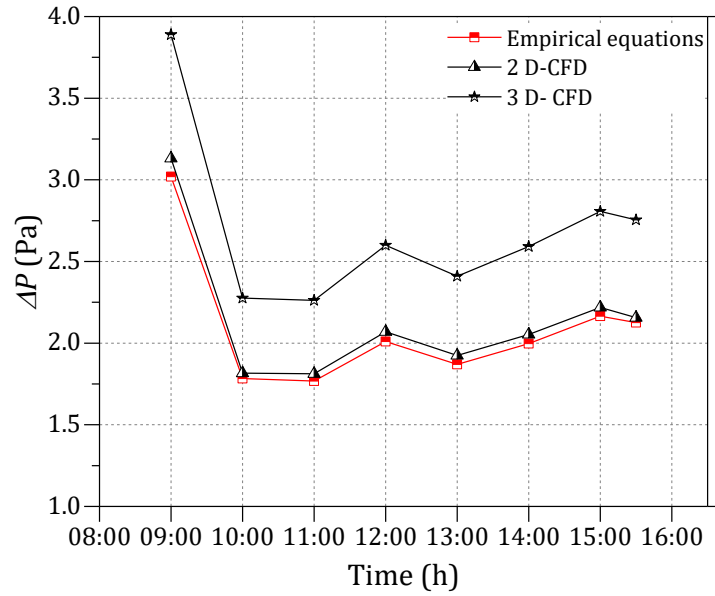
Figure 16. A comparison among 2D CFD, 3D CFD and empirical equations versus 09:00–16:00 hrs for the pressure drop estimated for design model C-I (single duct double pass U-flow design without Cans) using the data presented in Table 3.

Table 7. A comparison among 2D CFD, 3D CFD and empirical equations for the pressure drop estimated for design model C-I.

Empirical equations	2D-CFD	3D-CFD	E_1	E_2
3.01935	3.1316	3.8308	22.3578	3.58443
1.7835	1.816	2.2643	21.6354	1.789648
1.76834	1.8119	2.2505	21.81714	2.404106
2.00915	2.0695	2.5802	22.71311	2.916163
1.86987	1.925	2.3948	22.39593	2.863896
1.9968	2.053	2.5728	22.96296	2.737457
2.16472	2.2184	2.7824	22.89236	2.419762
2.1255	2.1559	2.7318	22.85777	1.410084

4. Conclusions

Numerical and experimental investigations were conducted to assess the performance of the double duct single pass solar air collector with recycled aluminium cans (RAC). The numerical study was built based on the finite element method provided by COMSOL Multiphysics V5.3a. The experiments were conducted in the western part of Iraq, Ar–Ramadi City (longitude: 33.25° N; latitude: 43.18° E) under clear sky and almost identical

weather conditions on 23rd (model C-I) and 27th (model C-II) February and 2nd (model C-III) March between 09:00 and 15:30. The average flowrates were 0.096 kg s^{-1} for model C-I, 0.088 for model C-II kg s^{-1} and 0.0819 kg s^{-1}. The comparative analysis of this work led to the following findings:

- Numerically, the U-flow offers better thermal performance than co-current and counter-current flow designs. Therefore, the U-flow model was chosen to be implemented in experimental studies.

- Thermal and hydrodynamic performance of numerical modelling is found to be in line with experiments (U-flow, model C-I).

- The increase in the thermal performance of U-flow model gave an increase in pressure drop, but the thermal efficiency was still higher compared to models A and B.

- The staggered arrangement (model C-III) had the highest thermal efficiency compared to the in-line (model C-II) and plain (model C-I) models.

- The in-line configuration (model C-II) had a lower efficiency compared to the staggered configuration (model C-III), even though the number of RACs and the mass flowrate were higher.

Acknowledgements

References

[1] A. Saxena and A. El-Sebaii, "A thermodynamic review of solar air heaters," *Renewable and Sustainable Energy Reviews,* vol. 43, pp. 863-890, 2015.

[2] M. Aktaş, A. Sözen, A. D. Tuncer, E. Arslan, M. Koşan, and O. Çürük, "Energy-Exergy Analysis of A Novel Multi-Pass Solar Air Collector With Perforated Fins," *International Journal of Renewable Energy Development,* vol. 8, pp. 47-55, 2019.

[3] B. A. Zvirin, Y, "A novel algorithm to investigate conjugate heat transfer in transparent insulation: application to solar collectors," *Numerical Heat Transfer: Part A: Applications,* vol. 35, pp. 757-777, 1999.

[4] A. S. Yadav and J. Bhagoria, "A numerical investigation of square sectioned transverse rib roughened solar air heater," *International Journal of Thermal Sciences,* vol. 79, pp. 111-131, 2014.

[5] M. Farshchimonfared, J. Bilbao, and A. Sproul, "Channel depth, air mass flow rate and air distribution duct diameter optimization of photovoltaic thermal (PV/T) air collectors linked to residential buildings," *Renewable Energy,* vol. 76, pp. 27-35, 2015.

[6] W. Fan, G. Kokogiannakis, and Z. Ma, "A multi-objective design optimisation strategy for hybrid photovoltaic thermal collector (PVT)-solar air heater (SAH) systems with fins," *Solar Energy,* vol. 163, pp. 315-328, 2018.

[7] İ. T. Toğrul and D. Pehlıvan, "The performance of a solar air heater with conical concentrator under forced convection," *International journal of thermal sciences,* vol. 42, pp. 571-581, 2003.

[8] S. Rhee and D. Edwards, "Laminar entrance flow in a flat plate duct with asymmetric suction and heating," *Numerical heat transfer,* vol. 4, pp. 85-100, 1981.

[9] A. Kabeel, M. H. Hamed, Z. Omara, and A. Kandeal, "Influence of fin height on the performance of a glazed and bladed entrance single-pass solar air heater," *Solar Energy,* vol. 162, pp. 410-419, 2018.

[10] H. K. Ghritlahre and R. K. Prasad, "Investigation of thermal performance of unidirectional flow porous bed solar air heater using MLP, GRNN, and RBF models of ANN technique," *Thermal Science and Engineering Progress,* vol. 6, pp. 226-235, 2018.

[11] N. Moummi, S. Youcef-Ali, A. Moummi, and J. Desmons, "Energy analysis of a solar air collector with rows of fins," *Renewable Energy,* vol. 29, pp. 2053-2064, 2004.

[12] R. Nadda, R. Kumar, A. Kumar, and R. Maithani, "Optimization of single arc protrusion ribs parameters in solar air heater with impinging air jets based upon PSI approach," *Thermal Science and Engineering Progress,* vol. 7, pp. 146-154, 2018.

[13] R. Maithani, A. Silori, J. Rana, and S. Chamoli, "Numerical analysis of heat transfer and fluid flow of a wavy delta winglets in a rectangular duct," *Thermal Science and Engineering Progress,* vol. 2, pp. 15-25, 2017.

[14] A. Kumar and A. Layek, "Thermo-hydraulic performance of solar air heater having twisted rib over the absorber plate," *International Journal of Thermal Sciences,* vol. 133, pp. 181-195, 2018.

[15] A. Saravanan. and S. Jaisankar, "Heat transfer augmentation techniques in forced flow V-trough solar collector equipped with V-cut and square cut twisted tape,," *International Journal of Thermal Sciences,* vol. 140, pp. 59-70, 1// 2019.

[16] H. Fugmann, L. Schnabel, and B. Frohnapfel, "Heat transfer and pressure drop correlations for laminar flow in an in-line and staggered array of circular cylinders," *Numerical Heat Transfer, Part A: Applications,* vol. 75, pp. 1-20, 2019.

[17] B. S. Romdhane, "The air solar collectors: comparative study, introduction of baffles to favor the heat transfer," *Solar Energy,* vol. 81, pp. 139-149, 2007.

[18] A. S. Yadav and J. Bhagoria, "A numerical investigation of turbulent flows through an artificially roughened solar air heater," *Numerical Heat Transfer, Part A: Applications,* vol. 65, pp. 679-698, 2014.

[19] H. Esen, "Experimental energy and exergy analysis of a double-flow solar air heater having different obstacles on absorber plates," *Building and Environment,* vol. 43, pp. 1046-1054, 2008.

[20] C. Prabha and S. Sharma, "Thermal Performance Prediction Of Extended Absorber Solar Air Heater," in *Proceedings 20th National and 9th ISHMT-ASME Heat and Mass Transfer conference*, 2010, pp. 1120-1124.

[21] S. Krishnananth and K. K. Murugavel, "Experimental study on double pass solar air heater with thermal energy storage," *Journal of King Saud University-Engineering Sciences,* vol. 25, pp. 135-140, 2013.

[22] R. Karwa and V. Srivastava, "Thermal performance of solar air heater having absorber plate with v-down discrete rib roughness for space-heating applications," *Journal of Renewable Energy,* vol. 2013, 2013.

[23] F. Chabane, N. Moummi, S. Benramache, D. Bensahal, and O. Belahssen, "Collector efficiency by single pass of solar air heaters with and without using fins," *Engineering Journal (Eng. J.),* vol. 17, pp. 43-55, 2013.

[24] L. S. Paraschiv, S. Paraschiv, and I. V. Ion, "Experimental and theoretical analyses on thermal performance of a solar air collector," *Environmental Engineering & Management Journal (EEMJ),* vol. 13, 2014.

[25] F. Chabane, N. Moummi, and S. Benramache, "Experimental study of heat transfer and thermal performance with longitudinal fins of solar air heater," *Journal of advanced research,* vol. 5, pp. 183-192, 2014.

[26] R. Tyagi, R. Ranjan, and K. Kishore, "Performance studies on flat plate solar air heater subjected to various flow patterns," *Applied Solar Energy,* vol. 50, pp. 98-102, 2014.

[27] M. Abuşka and M. B. Akgül, "Experimental study on thermal performance of a novel solar air collector having conical springs on absorber plate," *Arabian Journal for Science and Engineering,* vol. 41, pp. 4509-4516, 2016.

[28] B. Ramani, A. Gupta, and R. Kumar, "Performance of a double pass solar air collector," *Solar Energy,* vol. 84, pp. 1929-1937, 2010.

[29] A. Priyam and P. Chand, "Thermal and thermohydraulic performance of wavy finned absorber solar air heater," *Solar Energy,* vol. 130, pp. 250-259, 2016.

[30] R. K. Ravi and R. Saini, "Experimental investigation on performance of a double pass artificial roughened solar air heater duct having roughness elements of the combination of discrete multi V shaped and staggered ribs," *Energy,* vol. 116, pp. 507-516, 2016.

[31] G. Alvarez, J. Arce, L. Lira, and M. Heras, "Thermal performance of an air solar collector with an absorber plate made of recyclable aluminum cans," *Solar Energy,* vol. 77, pp. 107-113, 2004.

[32] A. Mohamad, "High efficiency solar air heater," *Solar energy,* vol. 60, pp. 71-76, 1997.

[33] B. Parker, M. Lindley, D. Colliver, and W. Murphy, "Thermal performance of three solar air heaters," *Solar Energy,* vol. 51, pp. 467-479, 1993.

[34] M. Sodha and R. Chandra, "Solar drying systems and their testing procedures: a review," *Energy Conversion and Management,* vol. 35, pp. 219-267, 1994.

[35] S. J. B. Hale, *Methods of testing to determine the thermal performance of solar collectors*: Ashrae, 1986.

[36] K. Altfeld, W. Leiner, and M. Fiebig, "Second law optimization of flat-plate solar air heaters Part I: The concept of net exergy flow and the modeling of solar air heaters," *Solar Energy,* vol. 41, pp. 127-132, 1988.

[37] F. Ozgen, M. Esen, and H. Esen, "Experimental investigation of thermal performance of a double-flow solar air heater having aluminium cans," *Renewable Energy,* vol. 34, pp. 2391-2398, 2009.

[38] H. Esen, F. Ozgen, M. Esen, and A. Sengur, "Artificial neural network and wavelet neural network approaches for modelling of a solar air heater," *Expert systems with applications,* vol. 36, pp. 11240-11248, 2009.

[39] S. Chamoli, R. Chauhan, N. Thakur, and J. Saini, "A review of the performance of double pass solar air heater," *Renewable and Sustainable Energy Reviews,* vol. 16, pp. 481-492, 2012.

[40] COMSOL Multiphysics Modeling Software 5.3a, "CFD Module Users Guide,," ed, 2018.

[41] D. C. Wilcox, *Turbulence modeling for CFD* vol. 2: DCW industries La Canada, CA, 1993.

[42] H. K. Versteeg and W. Malalasekera, *An introduction to computational fluid dynamics: the finite volume method*: Pearson Education, 2007.

[43] R. B. Bird, "Transport phenomena," *Applied Mechanics Reviews,* vol. 55, pp. R1-R4, 2002.

[44] S. Khanna, K. Reddy, and T. K. Mallick, "Optimization of finned solar photovoltaic phase change material (finned pv pcm) system," *International Journal of Thermal Sciences,* vol. 130, pp. 313-322, 2018.

[45] K. Sukhatme and S. P. Sukhatme, *Solar energy: principles of thermal collection and storage*: Tata McGraw-Hill Education, 1996.

[46] T. L. Bergman, F. P. Incropera, and A. S. Lavine, *Fundamentals of heat and mass transfer*: John Wiley & Sons, 2011.

[47] OGIMET. (2019). *Professional information about meteorological conditions in the world*. Available: http://www.ogimet.com/gsynres.phtml.en

[48] S. s. s. radiation. (2019). *data-helioclim-3 archives for free feb*. Available: http://www.soda-pro.com/web-services/radiation/helioclim-3-archives-for-free

[49] H. A. S. H. ASHRAE, "HVAC Applications Handbook," *IP Edition,* 2011.

[50] A. Schack, "Industrial heat transfer," *Verlag Stahleisen M B H, Dusseldorf. 1970, 464 P,* 1970.

[51] J. A. Duffie and W. A. Beckman, *Solar engineering of thermal processes*: John Wiley & Sons, 2013.

[52] S. T. Buisan, C. Azorin-Molina, and Y. Jimenez, "Impact of two different sized Stevenson screens on air temperature measurements," *International Journal of Climatology,* vol. 35, pp. 4408-4416, 2015.

[53] (2018). *LUTRON EM-9000 ENVIRONMENT METER, + Humidity, Anemometer, Light, type K/J*. Available: http://www.lutronmalaysia.com/index.php/item/1085-thermometers-thermocouple/5065-lutron-em-9000-environment-meter-humidity-anemometer-light-type-k-j

[54] Renewable Energy Research Center. (2018, March, 18,). *Install a solar tracking system the first of its kind in Iraq,* . Available: http://www.uoanbar.edu.iq/RERCenter/English/CMS.php?ID=33

[55] S. Rai, P. Chand, and S. Sharma, "Evaluation of thermo hydraulic effect on offset finned absorber solar air heater," *Renewable Energy,* vol. 125, pp. 39-54, 2018.

[56] A. A. Hegazy, "Comparative study of the performances of four photovoltaic/thermal solar air collectors," *Energy Conversion and Management,* vol. 41, pp. 861-881, 2000.

[57] (2018). *Friction Factor for Laminar Flow*. Available: https://www.nuclear-power.net/nuclear-engineering/fluid-dynamics/major-head-loss-friction-loss/friction-factor-for-laminar-flow/

[58] R. L. Daugherty, *Fluid mechanics with engineering applications*: Tata McGraw-Hill Education, 1989.

[59] D. F. Young, B. R. Munson, T. H. Okiishi, and W. W. Huebsch, *A brief introduction to fluid mechanics*: John Wiley & Sons, 2010.

[60] M. Ahmed-Dahmane and A. Z. Malek, Tahar "Design and analysis of a BIPV/T system with two applications controlled by an air handling unit," *Energy Conversion and Management,* vol. 175, pp. 49-66, 2018.

[61] K. E. Amori and M. A. Abd-AlRaheem, "Field study of various air based photovoltaic/thermal hybrid solar collectors," *Renewable Energy,* vol. 63, pp. 402-414, 2014.

[62] D. N. Moriasi, J. G. Arnold, M. W. Van Liew, R. L. Bingner, R. D. Harmel, and T. L. Veith, "Model evaluation guidelines for systematic quantification of accuracy in watershed simulations," *Transactions of the ASABE,* vol. 50, pp. 885-900, 2007.

[63] Z. Zhang, W. Zhang, Z. J. Zhai, and Q. Y. Chen, "Evaluation of various turbulence models in predicting airflow and turbulence in enclosed environments by CFD: Part 2—Comparison with experimental data from literature," *Hvac&R Research,* vol. 13, pp. 871-886, 2007.

[64] I. Guarracino, A. Mellor, N. J. Ekins-Daukes, and C. N. Markides, "Dynamic coupled thermal-and-electrical modelling of sheet-and-tube hybrid photovoltaic/thermal (PVT) collectors," *Applied Thermal Engineering,* vol. 101, pp. 778-795, 2016.

[65] M. S. Owen and H. E. Kennedy, "ASHRAE handbook: fundamentals," *SI edition, ASHRAE,* 2009.

[66] M. Gupta and S. Kaushik, "Performance evaluation of solar air heater having expanded metal mesh as artificial roughness on absorber plate," *International Journal of Thermal Sciences,* vol. 48, pp. 1007-1016, 2009.

[67] B. Brinkworth, "Estimation of flow and heat transfer for the design of PV cooling ducts," *Solar Energy,* vol. 69, pp. 413-420, 2000.

[68] M. Ansari and M. Bazargan, "Optimization of flat plate solar air heaters with ribbed surfaces," *Applied Thermal Engineering,* vol. 136, pp. 356-363, 2018.

[69] R. M. Manglik and A. E. Bergles, "Heat transfer and pressure drop correlations for the rectangular offset strip fin compact heat exchanger," *Experimental Thermal and Fluid Science,* vol. 10, pp. 171-180, 1995.